

④ a

AD-A277 364



251600-4-F

Final Technical Report

VALIDATION SUPPORT OF THE ERIM OCEAN MODEL

M. A. True

February 1994

Naval Research Laboratory
4555 Overlook Avenue SW
Washington, DC 20375

DTIC
ELECTE
MAR 24 1994
S E D

3086

94-09204



Contract No. N00014-93-C-2019

DTIC QUALITY INSPECTED 1

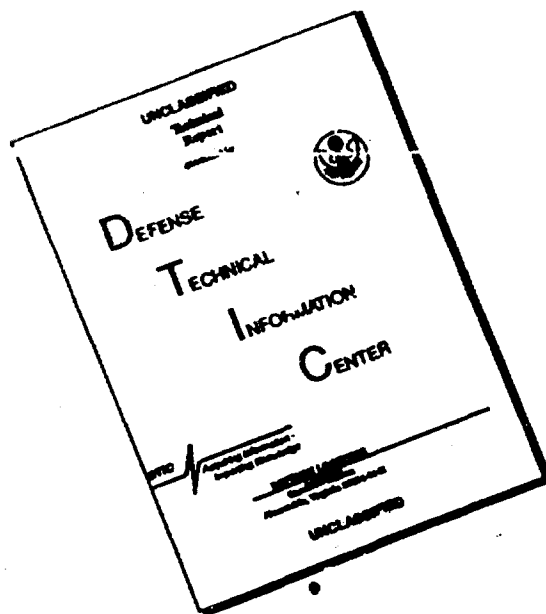


P.O. Box 134001
Ann Arbor, MI 48113-4001

94 2 23 9 5 8

Approved for public sale

DISCLAIMER NOTICE



**THIS DOCUMENT IS BEST
QUALITY AVAILABLE. THE COPY
FURNISHED TO DTIC CONTAINED
A SIGNIFICANT NUMBER OF
PAGES WHICH DO NOT
REPRODUCE LEGIBLY.**

1. Report No. 251600-4-F	2. Government Accession No.	3. Recipient's Catalog No.	
4. Title and Subtitle Validation Support of the ERIM Ocean Model		5. Report Date 28 Feb. 94	
		6. Performing Organization Code	
7. Author(s) M.A. True		8. Performing Organization Report No. 251600-4-F	
9. Performing Organization Name and Address Environmental Research Institute of Michigan (ERIM) P.O. Box 134001 Ann Arbor, MI 48113-4001		10. Work Unit No.	
		11. Contract or Grant No. N00014-93-C-2019	
12. Sponsoring Agency Name and Address Naval Research Laboratory 4555 Overlook Avenue S.W. Washington, DC 20375		13. Type of Report and Period Covered Technical Report 4 Feb 93 thru 3 Feb 94	
		14. Sponsoring Agency Code	
15. Supplementary Notes			
<p>16. Abstract</p> <p>The ERIM Ocean Model (EOM) is a comprehensive program for the simulation of SAR images of the ocean surface. EOM was delivered to NRL and integrated into the NASE Modeling System in 1991. The purpose of the NASE-EOM module is to simulate ocean surface effects as seen by SAR sensors.</p> <p>The purpose of the validation phase of the NASE-EOM project was to determine which of EOM's physics are reliable and which physics need improvement. To that end, a series of validation tests were run using NASE-EOM. For the Code-to-Theory test, the action spectral density equation was solved in EOM and compared with the linear solution. The results showed some numerical diffusion in EOM's solution which were reduced with finer spectral grid spacing. The Code-to-Code comparison consisted of a series of feature tables. The final validation test was the Code-to-Data comparison. The 11 test cases were run on the NASE Modeling System at NRL and the simulations were compared to experimental data. The simulated SAR signals were similar to each other and to the data for most test cases, but the simulated clutter had different appearances in the SAR codes due to differences in the simulation of the propagation of the waves during the SAR imaging time, the averaging to reduce the speckle, and the angular dependence of the equilibrium wave height spectrum.</p>			
17. Key Words SAR, Simulation Ocean Surface Hydrodynamics		18. Distribution Statement Unlimited	
19. Security Classif. (of this report) Unclassified	20. Security Classif. (of this page) Unclassified	21. No. of Pages 35	22. Price

CONTENTS

LIST OF FIGURES iii

LIST OF TABLES iv

1.0 INTRODUCTION 1

2.0 VALIDATION SUPPORT OF THE ERIM OCEAN MODEL 3

 2.1. REVIEW OF THE ERIM OCEAN MODEL. 3

 2.2. CODE-TO-THEORY COMPARISONS 6

 2.3. CODE-TO-CODE COMPARISONS. 9

 2.4. CODE-TO-DATA COMPARISONS. 13

3.0 CONCLUSIONS 17

4.0 REFERENCES 18

APPENDIX A. ERIM OCEAN MODEL INPUT FILE FOR VALIDATION TEST. . . 19

APPENDIX B. GEOMETRY FOR NASE VALIDATION TEST CASES..... 22

Accession For	
NTIS	<input checked="" type="checkbox"/>
CRA&I	<input type="checkbox"/>
DTIC	<input type="checkbox"/>
TAB	<input type="checkbox"/>
Unannounced	<input type="checkbox"/>
Justification	
By	
Distribution /	
Availability Codes	
Dist	Avail and/or Special
A-1	

LIST OF FIGURES

1.	Flowchart for the ERIM Ocean Model (EOM)	3
2.	Comparison of EOM Solution with the Linearized Analytic Solution	7
3.	Increased EOM Accuracy With 3.7° Angular Grid Spacing	7
4.	The Along Wind Equilibrium Wave Height Spectrum for a Wind Speed of 4.2 m/s	14
5.	The Angular Dependence of the Wave Height Spectrum at the Peak Wavenumber for RHS=0 and RHS=9 Cases	14
6.	The Exponential Distribution of Speckle Intensity	16
B-1.	EOM Geometry for 109-4	23
B-2.	EOM Geometry for 109-5	24
B-3.	EOM Geometry for 115-3	25
B-4.	EOM Geometry for 222-4	26
B-5.	EOM Geometry for 506-3	27
B-6.	EOM Geometry for 506-4	28
B-7.	EOM Geometry for 506-5	29
B-8.	EOM Geometry for 914-4	30
B-9.	EOM Geometry for 914-5	31

LIST OF TABLES

1.	Domain	9
2.	Input Signature Fields	10
3.	Noise Fields	10
4.	Wave Action	11
5.	SAR Image Generation	12

1.0 INTRODUCTION

The ERIM Ocean model (EOM) is a comprehensive program for the simulation of SAR images of the ocean surface. EOM was delivered to NRL and integrated into the NASE Modeling System in 1991. The purpose of the NASE-EOM module is to simulate ocean surface effects as seen by SAR sensors. To this end, the relevant physics must be included and validated with experimental data. The ultimate goal of the validation effort is to determine which SAR observables are modeled correctly and which modeling physics needs improvement.

The purpose of the current phase of the NASE-EOM modeling effort was to validate the ERIM Ocean Model in the context of the NASE Modeling System. The Validation Study was comprised of a number of subtasks reflecting the fact that validation can be performed on a number of different levels: 1) Code-to-Theory, 2) Code-to-Code, and 3) Code-to-Data. The different levels are discussed below.

Code-to-Theory

The exact analytic solution for the general ocean surface dynamics problem is not known. Thus, there is a need for the numerical solutions generated by EOM. There are, however, exact solutions for idealized situations where some physical parameters are very large or very small and all the spatial variations are in one dimension. The use of these analytic test cases allows the numerical accuracy of EOM to be evaluated. Such analytic cases were compared to EOM calculations and the results showed that EOM's accuracy increased as more grid points were added in spectral space.

Code-to-Code

NASE has several modules which perform nearly identical modelling functions. The first step in comparing modules which solve the same physical problem is to construct feature tables which detail the physics, numerical methods, inputs, and outputs of each of the codes. Such a set of tables was generated for EOM and delivered to NRL. The tables can be used in conjunction with the analytic test cases described in the Code-to-Theory section to determine which code's numerical implementation is more accurate. The tables also show unique physics in EOM which can be used in a sensitivity study to determine where the physical effect is important in parameter space. In addition to

feature table comparisons, direct comparison between outputs were made. To support the direct comparison of results ERIM modified the EOM outputs in order to exactly match the outputs of other SAR codes.

Code to Data

The final validation step was the end-to-end execution of NASE including comparison with experimental data. The validation test cases were chosen from previous experiments which were well characterized. ERIM provided input diagrams which characterized the critical input parameters. The 11 validation test cases were analyzed at a NASE working group meeting and the EOM results can be summarized as follows. The signal modeling appeared to be similar for all SAR codes and in reasonable agreement with the data. The clutter and speckle appeared to be different in the different SAR modules. Further analysis described in this report showed that this was due in part to the following differences in the SAR codes: 1) the equilibrium distributions used; 2) the SAR imaging effects included (e.g. time dependent effects); and 3) the speckle averaging employed.

The organization of the report is as follows. First, the ERIM Ocean Model will be reviewed. Then the validation task results will be described in the following order: 1) Code-to-Theory; 2) Code-to-Code; and 3) Code-to-Data. Finally, the conclusions of the validation effort will be presented.

2.0 VALIDATION SUPPORT OF THE ERIM OCEAN MODEL

2.1. REVIEW OF THE ERIM OCEAN MODEL

The ERIM Ocean Model (EOM) is a comprehensive set of computer modules which produce simulated SAR imagery of ocean features (Lyzenga and Bennett, 1988). The flowchart in Figure 1 shows the input, output, and processing structure of EOM.

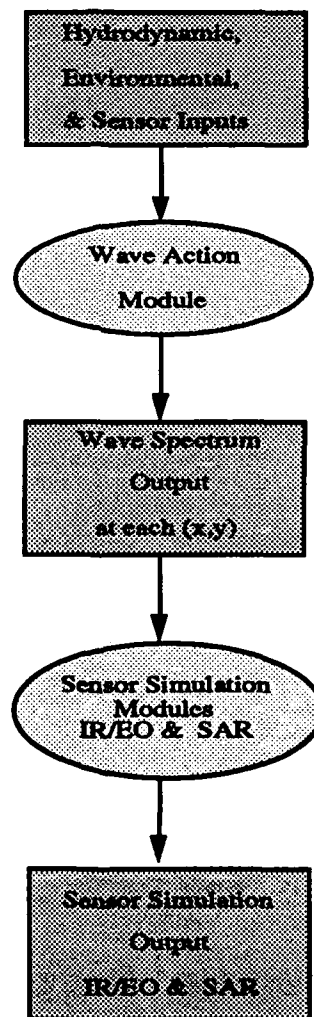


Figure 1. Flowchart for the ERIM Ocean Model (EOM).

The first processing module is the wave action module. Its inputs are the 2-D surface currents and the environmental conditions. In this module EOM integrates the nonlinear wave action equation to compute the variations in action spectral density in the presence of variable currents. It does this on a 2-D spatial and wavenumber grid. EOM's action spectral equation is a full nonlinear 2-D description of the ocean surface wave physics:

$$\begin{aligned} & (c_{gx}+u)\frac{\partial N}{\partial x} - (k_x\frac{du}{dx} + k_y\frac{dv}{dx})\frac{\partial N}{\partial k_x} + \\ & (c_{gy}+v)\frac{\partial N}{\partial y} - (k_x\frac{du}{dy} + k_y\frac{dv}{dy})\frac{\partial N}{\partial k_y} = F_s(N) \end{aligned} \quad (1)$$

where c_{gx} and c_{gy} are the group velocity components, N is the action spectral density, u and v are the currents, and $F_s(N)$ is the net sum of all the known sources and sinks of wave energy. The action spectral density is related to the more familiar wave height spectrum, S , by the relation: $N = \rho c S$ where c is the phase speed and ρ is the density of water. The action spectral equation is solved in EOM by an upwind differencing scheme.

For the validation studies described in this report, the net source function was assumed to be of the form discussed in detail by Lyzenga (1991):

$$F_s(N) = \Pi + \beta N - \beta_d N - \gamma N^2. \quad (2)$$

The terms in this equation represent, respectively, the Phillips growth mechanism, the exponential wind growth mechanism, the viscous damping, and the nonlinear dissipation which is intended to incorporate the effects of wave breaking in limiting the wave growth. Equation 2 is essentially a generalization of the Hughes (1978) formulation.

Many of the terms in the net source function are highly uncertain. We have used the exponential growth parameter suggested by Snyder et al. (1981),

$$\beta = 0.0003 [U/c \cos(\phi - \phi_w) - 1] \omega, \quad (3)$$

where U is the wind speed, $\phi - \phi_w$ is the direction relative to the wind, and ω is the wave frequency. The loss rate in Equation 2, $\beta_d = 4 \nu k^2$, is the well-known viscous dissipation. In order to estimate the other two terms, Phillips constant growth and nonlinear wavebreaking (Phillips 1980 and 1985), we have assumed that for wavenumbers near the spectral peak, the equilibrium spectrum is the result of an approximate balance between these two terms, and that the equilibrium spectrum has the Pierson-Moskowitz (1964) form, so that

$$\Pi = \gamma N_{PM}^2 \quad (4)$$

where $N_{PM} = \rho c S_{PM}$ and S_{PM} is the Pierson-Moskowitz height spectrum (converted to wavenumber coordinates) with a $\cos^4[(\phi - \phi_w)/2]$ azimuth dependence. This leaves one unknown parameter, γ , which may be re-written as $\gamma = (\omega k^4 / \rho c) \gamma_o$ where γ_o is a dimensionless constant.

The total equilibrium spectrum is given by the solution of the equation $F_S(N_o) = 0$, which yields

$$N_o = \frac{(\beta - \beta_d) + [(\beta - \beta_d)^2 + 4 \gamma \Pi]^{1/2}}{2\gamma} \quad (5)$$

This results in a wind speed dependence at large wavenumbers, the magnitude of which depends on the constant γ_o . This parameter was chosen ($\gamma_o=1$) to match the wind speed dependence of the slope variance, as observed by Cox and Munk (1954).

Following the spectral processing, a description of the sensor and its resolution are input into EOM. If the sensor is a SAR, EOM uses the two-scale Bragg scattering theory to calculate the radar cross section (RCS). Next, a realization of the ocean surface is created to further modulate the RCS due to the tilting of the resolved ocean waves. Then the SAR phase history of the ocean surface is constructed. The resolved ocean waves are not propagated during the phase construction but the smearing due to the sub-resolution waves by their velocity variance is included. Then, EOM focuses the phase

history and outputs the simulated SAR image of the ocean surface phenomena. Intermediate results can also be output in order to determine which physical processes were dominant in the image formation.

2.2. CODE-TO-THEORY COMPARISON

The action spectral density equation (Eq. 1) can be solved when the current strain is small and, therefore, the fractional change of the equilibrium distribution, f , is also small. This can be verified 'a posteriori'. A further requirement is that the spatial variation be one dimensional. Details of the solution can be found in Lyzenga (1991). The solution for the perturbation, f , is

$$f = \frac{u'_0}{\beta_r} \sin(\phi) \left[\left[k \frac{\partial}{\partial k} \ln(N_0) \right] \cos(\phi) - \left[\frac{\partial}{\partial \phi} \ln(N_0) \right] \sin(\phi) \right] \quad (6)$$

where u'_0 is the current strain rate for the convergent current, β_r is the relaxation rate, N_0 is the equilibrium action distribution, and ϕ is the angle with respect to the current direction. This solution is in the highly damped limit. The equilibrium action distribution (from Eq. 5) is sufficiently complex that numerical derivatives are taken in evaluating 'f' in Equation 6.

The comparison of the EOM solution and the analytic result is given in Figure 2. The strain rate for this case was 0.0005 s^{-1} inside the linearly-ramped convergent current. The wavenumber, k , was chosen to be the Bragg wavenumber for C-band at 23° incidence angle. The errors in 'f' are larger outside $\pm 90^\circ$ of the wind direction because EOM solves for S . Specifically, the errors in S are small in the downwind direction even when the errors in f are large because $S = S_{eq}[1+f]$ and S_{eq} is small downwind. In other words, most of the spectral energy is within $\pm 90^\circ$ of the upwind direction. The difference between the EOM solution and the analytic solution within the important region, $\pm 90^\circ$ from the upwind direction, is shown in Figure 3. The cause of the error is the numerical diffusion which is inherent in the upwind differencing scheme used. One way to improve the accuracy is to reduce the grid spacing. This is shown in Figure 3. The grid spacing was halved and the accuracy was improved by a factor of 2. The mean relative error for the 3.7° grid spacing case was 10% which is acceptable given the uncertainties in the sources and sinks.

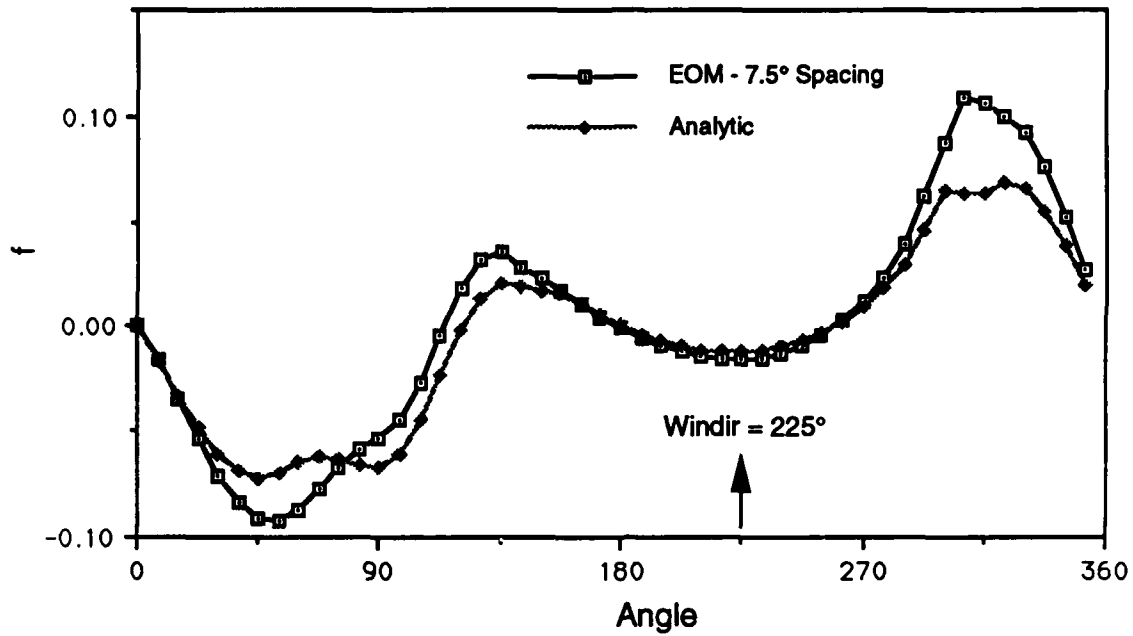


Figure 2. Comparison of EOM Solution with the Linearized Analytic Solution

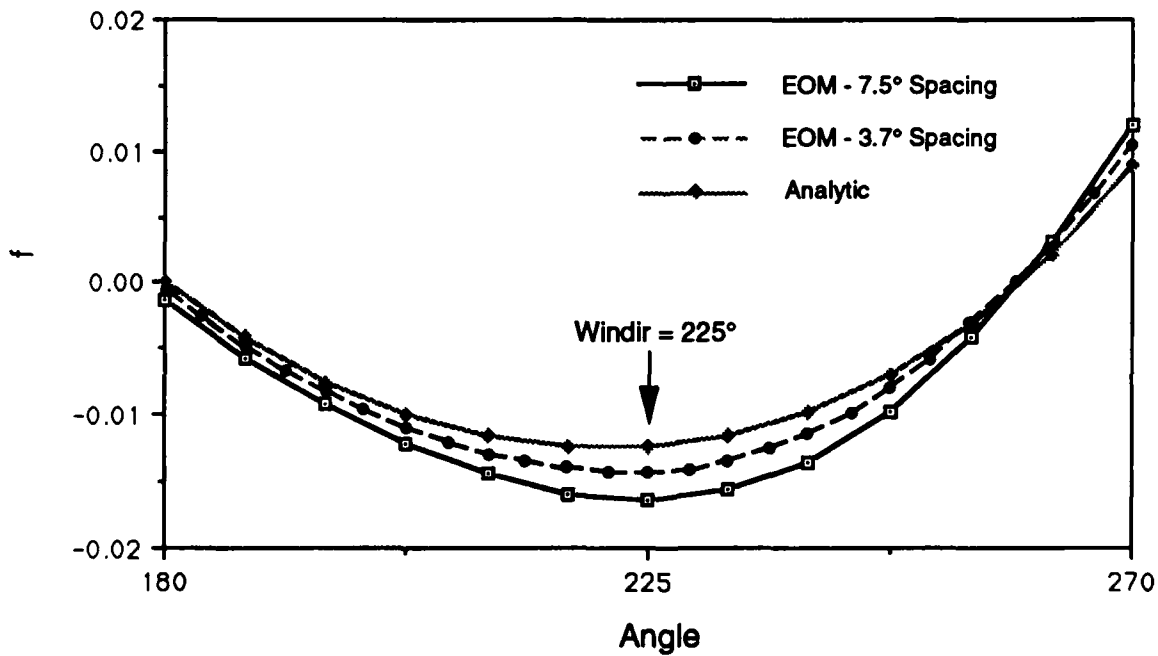


Figure 3. Increased EOM Accuracy With 3.7° Angular Grid Spacing.

The reason for the narrow grid spacing in angle is that the angular variation of the Pierson-Moskowitz distribution is $\cos^4[(\phi - \phi_w)/2]$ which changes rapidly for downwind directions. Reducing the grid spacing in k improved the accuracy for up to 64 wavenumbers but had little effect thereafter because the logarithmic derivative of the equilibrium spectrum is smooth. The spatial gridding had little effect because the current pattern was smooth and adequately sampled. The conclusion of this test is that the grid spacing must resolve the variations in the currents, sources, and sinks in both the spectral and spatial domains.

2.3 CODE-TO-CODE COMPARISONS

The ERIM Ocean Model was reviewed in Section 2.2. The SAIC and DTI SAR codes are reviewed in their respective final reports. For intercode comparisons it is useful to put the code descriptions in a common framework. As a first step to the intercode comparisons, feature tables were constructed. Naturally, the feature tables cannot be comprehensive. For instance, the tables do not show either implementation methods or the unique code capabilities. Different tables are defined for input, output, and physical process description. The table headings are: Domain, Input Signature Field, Noise Field, Wave Action Spectral Density, and RCS Model. Each table is followed by comments which address features not covered in the table.

Table 1. Domain

Grid Resolution	Variable
Typical Size	256 X 256 Spatial Domain 48 X 12 Spectral Domain
Fields on Grid: Input	U & V Currents, Turbulence, & Depth
Output	RCS, SAR Intensity, & others
Input Parameters	Environment, Sensor & Geometry

The domain depends not only on the data fields used but also on the resources of the host computer. This is particularly true of EOM. The unique capability of solving the full nonlinear wave action equation requires the entire 4D spectral-physical grid to be accessible in virtual memory. But the array sizes are large—50 Mbyte files are common. This can strain the virtual memory operating system since disk file space must be available for the virtual memory arrays. Another unique feature of EOM is that it uses two types of grids – a hydrodynamic grid and a sensor grid. EOM was written with outputs in the sensor coordinate system in order to compare them directly to SAR data, but this makes intercomparisons more difficult with codes that output data on the hydrodynamic grid.

Table 2. Input Signature Fields

Surface Elevation	Yes
Surface Velocity	Yes
Turbulence	Yes
Variable Depth	Yes
Moving or Stationary	Constant Velocity in X and Y

The 'Input Signature Fields' determine which 2D perturbations can be modeled. The most common signature field is the surface velocity. Next in importance is the effect of turbulence which requires the input of the 2D turbulent dissipation field. EOM's turbulence model is essentially an additional turbulent dissipation which is added to the usual viscous dissipation.

A capability which is unique to EOM is the modeling of variable ocean depth. The change of the dispersion relation near shore has major effects on the surface wave spectrum and propagation. EOM also includes a surfactant model, but it is presently not a spatially dependent input field. That is, the surfactant is assumed to cover the entire simulation area, but the 2D effect of the surface current on the surfactant is included.

Table 3. Noise Fields

Wind Wave Spectrum	Many User Choices
Swell	Yes
Generated Internally or Input	Spectrum Internal, Swell Input
Moving or Stationary	Stationary
Speckle (DOF)	One (from the SAR Processor)

The 'Noise Fields' produce the clutter from which the signal must be discriminated. It turns out that this is the area of greatest difference between the DTI, SIAC, and ERIM codes. The noise generation can be divided into two parts: 1) the physical source of the clutter and 2) the SAR imaging method. With respect to the physical source of the clutter, EOM has the widest choice of wind wave spectrums—they are all published analytic functions of windspeed and direction. But the lack of proof about which one is 'right' causes considerable uncertainty in the clutter output.

Turning to the SAR imaging method, the resolved waves are not propagated during the SAR synthesis in EOM. This causes them to be 'sharper' in the SAR image than the waves in the SIAC SAR code. However, the clutter model does include smearing due to the non-resolved waves—in fact, it includes non-stationary statistics in the phase history generation step which is not in the other codes. The non-stationary statistics simulate the sub-resolution scale waves particularly well.

Table 4. Wave Action

Sub-resolution and/or Resolved Waves	Both
Strain Due to	Currents
Linear or Nonlinear	Nonlinear
Steady or Time-dependent	Steady
RHS (forcing and damping)	7 Combinations of Wave Sources and Sinks
Beta	Hughes, Plant, Inoue, Lyzenga, Thompson
Numerical Method	Upwind on 4D grid
Output Fields	2D Spectrum at Each X-Y Grid Point

EOM solves the full nonlinear equation for many combinations of sources and sinks. This is particularly important when the current strain is large. However, no one source or sink model is fully accepted by the research community. The different models were based on analyses of different experiments. For example, Snyder's and Plant's beta

(growth rates) are both well known. The consensus is that Plant's is slightly better for short wavelengths and Snyder's is a better description for long wavelengths. But, the angular dependence of both Snyder's and Plant's beta are not well known. The inclusion of breaking waves is not implemented exactly for any code because it is very difficult to implement the exact wave-wave nonlinear interaction. The current EOM wavebreaking model is a quadratic function of the action spectral density.

Table 5. SAR Image Generation

Bragg & Specular	Both
Tilt Modulation	Yes
Hydro Modulation	For Long Wave Case
Composite Effects	Yes, 2-Scale
Range Foreshortening	No
Linearized Modulation	Nonlinear Composite
Limits of Validity:	Incidence Angle < 80°
Antenna Functions	Uniform Illumination

There is wide variation in the SAR imaging effects between the different SAR codes. For the static RCS all the codes have Bragg and specular effects. Tilt modulation is in EOM but velocity bunching is not. Hydro modulation is included for long waves whose currents are explicitly input. For sub-resolution waves, the velocity variance smearing is accounted for in the phase history generation. The displacement due to the motion in the current field is also included.

It is worth noting that user interface and code maintainability are not included in the above tables but they have significant effects on EOM's usefulness. EOM has its own command line interface with automatic log file generation and a modular design which is easy to maintain and add new features.

2.4 CODE-TO-DATA COMPARISONS

The NASE Modeling System was run end-to-end for 11 test cases and compared to experimental data. The NASE simulation runs were executed at NRL. The input files for the EOM module were supplied by ERIM. An example of an EOM input file for a test case is given in Appendix A. Difficulties in comparing the inputs and outputs of the various modules of NASE were caused by the use of different coordinate systems in the different modules which were developed separately. To facilitate the comparison of EOM parameters with the other modules, geometric diagrams for all the test cases were delivered to NRL. Although meant mostly for EOM documentation they became the standard by which all geometrical references were made (see Appendix B).

The signal structure was similarly modeled by all codes and agreed reasonably well with the experimental data (see the NASE Validation Final Report). As discussed in the Code-to-Theory section, the signal perturbation depends on the details of the equilibrium spectrum, the wind direction, current strain and direction, and wind speed. There were not enough test cases to fully discriminate between the different SAR codes on the basis of data comparison in this multi-dimensional parameter space.

The clutter had a significantly different appearance in the different SAR code outputs and the experimental data. The experimental data showed dark streaks (possibly) due to surfactants which were not included in any SAR code simulations. Note that EOM has the ability to perform surfactant simulations given the characteristics of the surfactant. Also, the simulated smearing in the azimuthal direction differed depending on the degree of wave motion included during the SAR image formation. EOM has an azimuthal smearing due to the sub-resolution waves' velocity variance but the long waves were not propagated during the SAR phase history formation and so they were relatively 'sharp' compared to the SAIC-SAR long waves.

The wind direction was more apparent from the clutter in the SIAC-SAR and DTI-SARSIM codes. As discussed in Sections 2.1 and 2.3, EOM has many source and sink formulations. The Lyzenga theory (1991) was used in this study. Figure 4 shows the wave height spectrum for the Lyzenga theory and the older Lyzenga-Bennett (1988) theory. There is some small difference at long wavelengths.

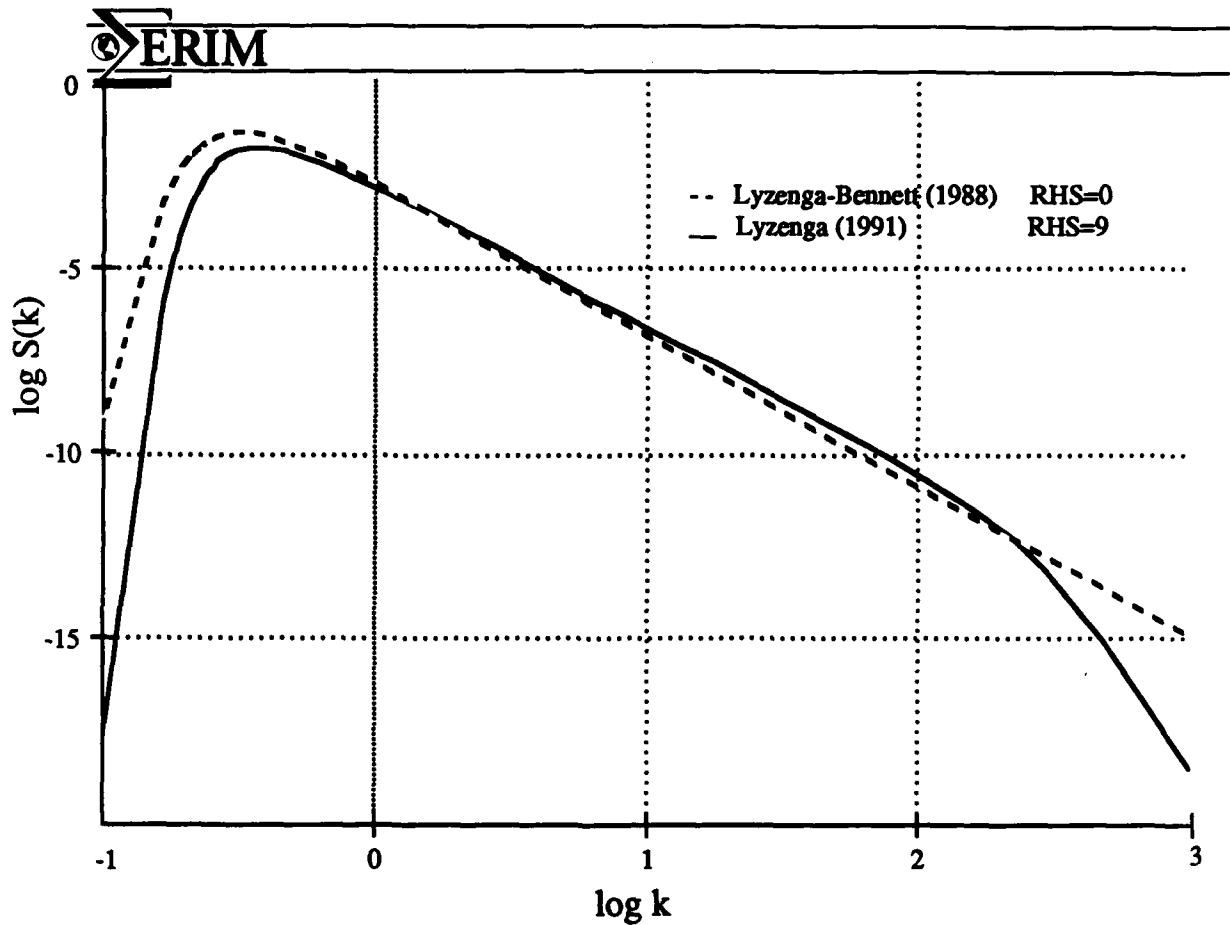


Figure 4. The Along Wind Equilibrium Wave Height Spectrum for a Wind Speed of 4.2 m/s.

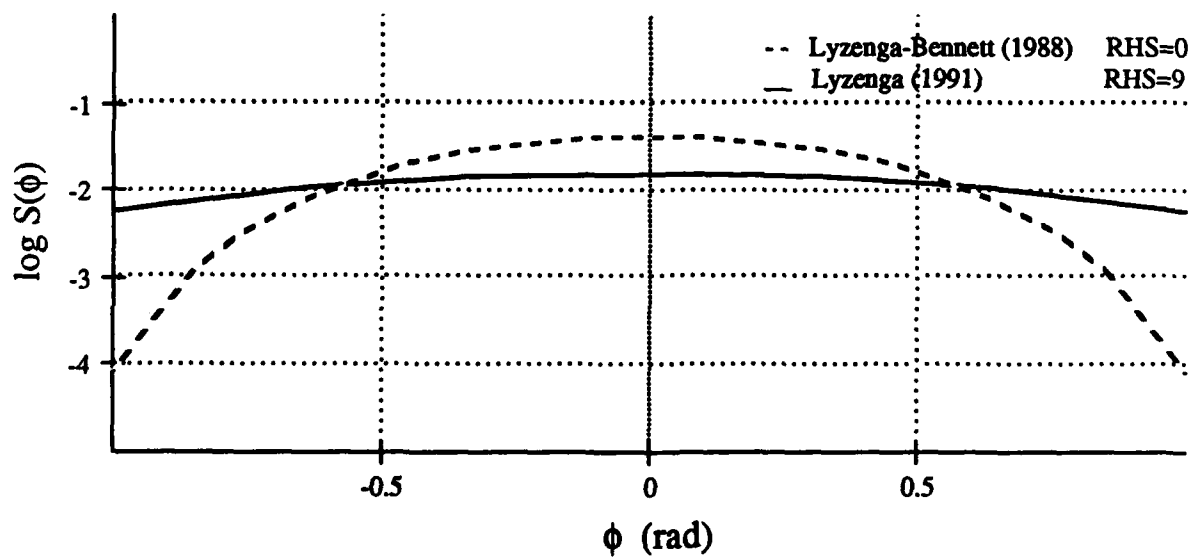


Figure 5. The Angular Dependence of the Wave Height Spectrum at the Peak Wavenumber ($\log k = -0.5$, $\lambda = 21$ m) for the RHS=0 and RHS=9 Cases.

A larger difference is in the cutoff at the large k in the Lyzenga theory due to the viscosity effect which is not in the older Lyzenga-Bennett (1988) theory. The cutoff effects the velocity variance and the radar cross section but it does not alter the long wave directional appearance.

The appearance of a preferred clutter direction is dependent on the angular width of the wave height spectrum. There appears to be a substantial difference between the SAR codes in the angular width of the equilibrium spectrum. A narrower angular spectrum gives a more directional appearance to the clutter. The equilibrium spectrum used in EOM had an effective cosine to the fourth power angular dependence for all ocean wavelengths. As shown in Figure 5, the older Lyzenga-Bennett theory has a narrower angular dependence for the long waves which would give the clutter a more directional appearance. The angular dependence of the older theory could be incorporated into the newer theory via the constant source term while still maintaining the better physical description of the short gravity-capillary waves.

Speckle in the EOM intensity image appeared to be stronger than in the other SAR intensity images. Since EOM generates speckle from the focussing of the phase history it is potentially more accurate than the other methods which impose a speckle distribution on the RCS image (including motion effects). The EOM SAR processor creates a single look high resolution image. To test its speckle properties, statistics were gathered on a 80 X 80 pixel region from an EOM-generated SAR image. The histogram of the results is shown in Figure 6. The graph shows that the intensity has an exponential distribution as expected from theory. The high resolution SAR image was contracted in the intensity domain to produce a final resolution equal to the experimental data. The other SAR codes used the statistics of an n -look distribution to generate speckle. This saves a lot of disk space since the high resolution image is not created but it may not be as accurate since the n -look theory assumes a uniform RCS distribution which is not true in either an averaged signal-clutter pixel or in an averaged clutter pixel which encompasses 1-5 meter waves whose RCS varies from crest to trough.

In conclusion, the Code-to-Data tests showed areas of substantial agreement between NASE-EOM and experimental data as well as areas where further testing and additional physics is required.

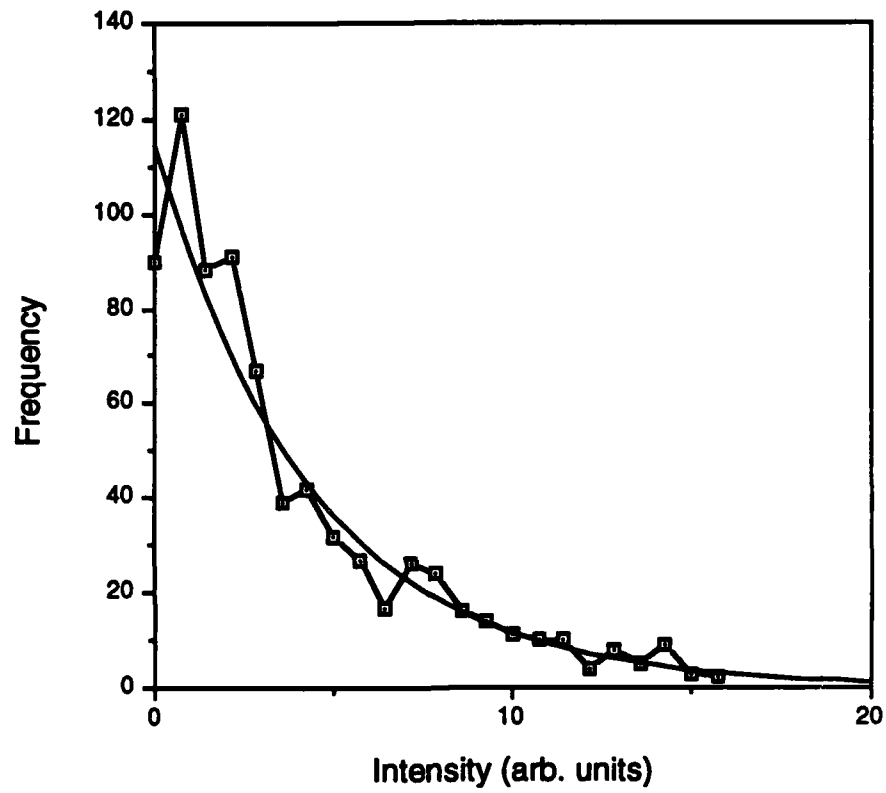


Figure 6. The Exponential Distribution of Speckle Intensity

3.0 CONCLUSIONS

The purpose of the validation phase of the NASE-EOM project was to determine which of EOM's physics are reliable and which need improvement. To that end, a series of validation tests were run using NASE-EOM. For the Code-to-Theory test, the action spectral density equation was solved in EOM and compared with the linear solution which is valid in the limit of small current shear. The results showed some numerical diffusion in EOM's solution which were reduced with finer spectral grid spacing. The Code-to-Code comparison consisted of a series of tables filled out similarly for all the NASE SAR codes. The tables differentiated between the physics included in each code. The tables show that the strengths of EOM are its variable depth, surfactant, and turbulence capabilities. Other key EOM features are its nonlinear action spectral equation solver, phase history generator, and SAR focusing algorithm. The final validation test was the Code-to-Data comparison. The eleven test cases were run on the NASE Modeling System at NRL and the simulations were compared to experimental data. The simulated SAR signals were similar to each other and to the data for most test cases, but the simulated clutter had different appearances in the SAIR-SAR, DTI-SARSIM, and ERIM-EOM codes. Some simulations matched the experimental clutter—others did not. The differences between the simulated clutter were due to differences in the simulation of the propagation of the waves during the SAR imaging time, the averaging to reduce the speckle, and the angular dependence of the equilibrium wave height spectrum.

4.0 REFERENCES

Cox, C. and W. Munk, Statistics of the sea surface derived from sun glitter, *J. Mar. Res.*, *13*, 198-227, 1954.

Hughes, B.A., The effects of internal waves on surface wind waves: Theoretical analysis, *J. Geophys. Res.*, *83*, 455-465, 1978.

Lyzenga, D. R. and J. R. Bennett, Full-spectrum modeling of synthetic aperture radar internal wave signatures, *J. Geophys. Res.*, *93*, 12345-12354, 1988.

Lyzenga, D. R., Interaction of short surface and electromagnetic waves with ocean fronts, *J. Geophys. Res.*, *96*, 10765-10772, 1991.

Phillips, O.M., *The Dynamics of the Upper Ocean*, 1st paperback ed., 336 pp. Cambridge University Press, New York, 1980.

Phillips, O.M., Spectral and statistical properties of the equilibrium range in wind generated gravity waves, *J. Fluid Mech.*, *156*, 505-531, 1985.

Pierson, W.J., and L. Moskowitz, A proposed spectral form for fully developed seas based on the similarity theory of S. A. Kitaigorodskii, *J. Geophys. Res.*, *69*, 5181-5190, 1964.

Plant, W.J. A two-scale model of short wind-generated waves and scatterometry, *J. Geophys. Res.*, *91*, 10735-10749, 1986.

Snyder, R.L., F.W. Dobson, J.A. Elliott, and R. D. Long, Array measurements of atmospheric pressure fluctuations above surface gravity waves, *J. Fluid Mech.*, *102*, 1-59, 1981.

APPENDIX A. ERIM OCEAN MODEL INPUT FILE FOR VALIDATION TEST

```
;  
; Case 109-4 EOM parameter file, April 12, 1993  
;  
; 'Simtype=general' for surface current input from external files  
; 'Hydrofile' parameter is the prefix of the surface current files  
;  
SIMTYPE=general  
HYDROFILE=eom109-4  
;  
; Hydro grid dimensions (pixels) in X and Y  
; Pixel dimensions (m) are in current file header  
;  
NX=256  
NY=128  
;  
; Grid dimensions in WAVENUMBER and ANGLE  
;  
NK=48  
NP=12  
;  
; Min and Max wavelength of ocean wave spectrum (m)  
; Min wavelength is smaller than Bragg wavelength of Radar frequency  
; Max wavelength is 2(wndspeed**2)  
;  
WLMIN=0.005  
WLMAX=11.000  
;  
; Surfactant pressure (dynes/cm)  
;  
P0=0.000  
;  
; Wind speed (m/s) and wind direction (deg)  
; Wind direction is the 'toward' direction counterclockwise wrt X-axis  
;  
WNDSPD=2.250  
WINDIR=232.00  
;  
; Doppler velocities (m/s) in X and Y  
; 'Udoplr' is the target velocity in the X-direction  
;  
UDOPLR=-3.00  
VDOPLR=0.000  
;  
; Water depth. DEEP=.True. for deep water dispersion relation
```

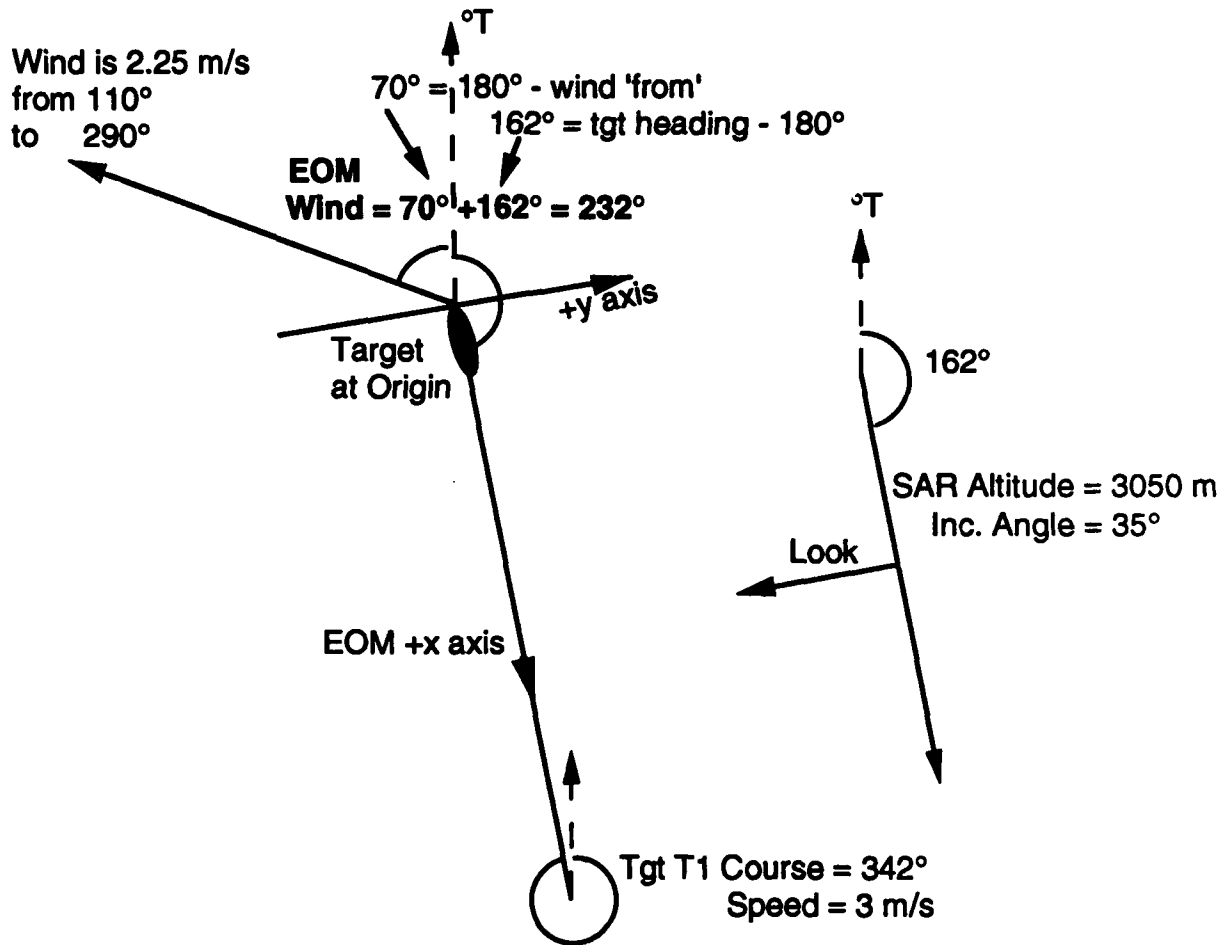
```
;  
DEEP=.True.  
;  
; 'Sensorfile' is the file name prefix for the sensor output  
;  
SENSORFILE=eom109-4-L-VV  
;  
; Electromagnetic frequency (GHz), Incidence angle  
; (degrees), water temperature (degrees centigrade) and  
; salinity (ppt)  
;  
EF=1.280  
INCANG=35.000  
TEMP=15.000  
SAL=35.000  
;  
; Number of rows and columns in the sensor simulation  
; Pixel dimensions (m) in the sensor simulation  
;  
NXCOLS=512  
NYROWS=128  
XPIXEL=6.000  
YPIXEL=6.000  
;  
; Origin of input and output grids (m)  
;  
XORGNI=0.000  
YORGNI=0.000  
XORGNO=0.000  
YORGNO=0.000  
;  
; 'Angrot' is the angle of the Look direction wrt the X-axis  
; of the hydro grid (counterclockwise in degrees)  
;  
ANGROT=270.0  
;  
; Additional SAR parameters for: Polarization, platform velocity (m/s),  
; range (m) = height/cos(inc), sensor output type, random no. seed,  
; number of antennas, right hand side, and I/O style.  
;  
POLAR=vv  
VEL=120.000  
RANGE=3723.000  
SENSOR=psar  
ISEED=1234567  
NAPT=1  
RHS=9  
IOSTYLE=nrl
```

```
;  
; Parameters which effect the SAR phase history and SAR processor  
;  
AZRES=1.000  
FILTFAC=1.000  
LCUT=1  
FOCUS=1.000  
;  
; The following options have been turned off:  
; dualbragg, save the complex image, long wave, internal wave,  
; multiple antennas, and turbulence  
;  
DUALBRAGG=.False.  
SAVECOMPLEX=.False.  
AMPLW=0.000  
WVLNLW=0.000  
UHUMP=0.000  
BAPT=0.0  
ZAPT=0.0  
TURB=.False.
```

APPENDIX B. GEOMETRY FOR NASE VALIDATION TEST CASES

Diagrams for the 9 validation test case geometries are given on the following pages.

EOM Geometry for 109-4



The EOM X-axis is defined by:

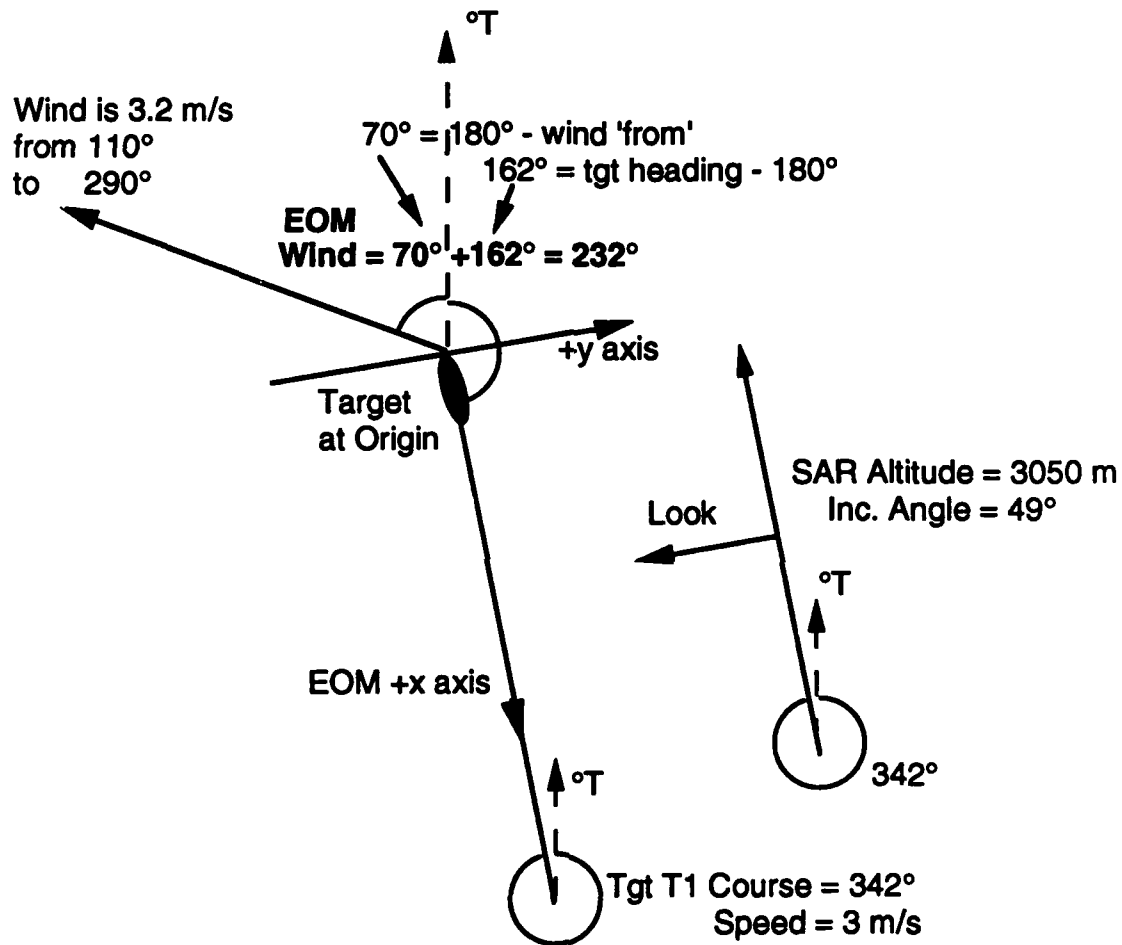
- Target at the origin
- Positive x-axis along track
- Target travel in the -x direction

The EOM angles are defined as:

- $\text{ANGROT} = 270^\circ = \text{angle of 'look' vector wrt x-axis (ccwise)}$
- $\text{WINDIR} = 232^\circ = \text{angle of wind 'to' vector wrt x-axis (ccwise)}$

Figure B-1. EOM Geometry for 109-4

EOM Geometry for 109-5



The EOM X-axis is defined by:

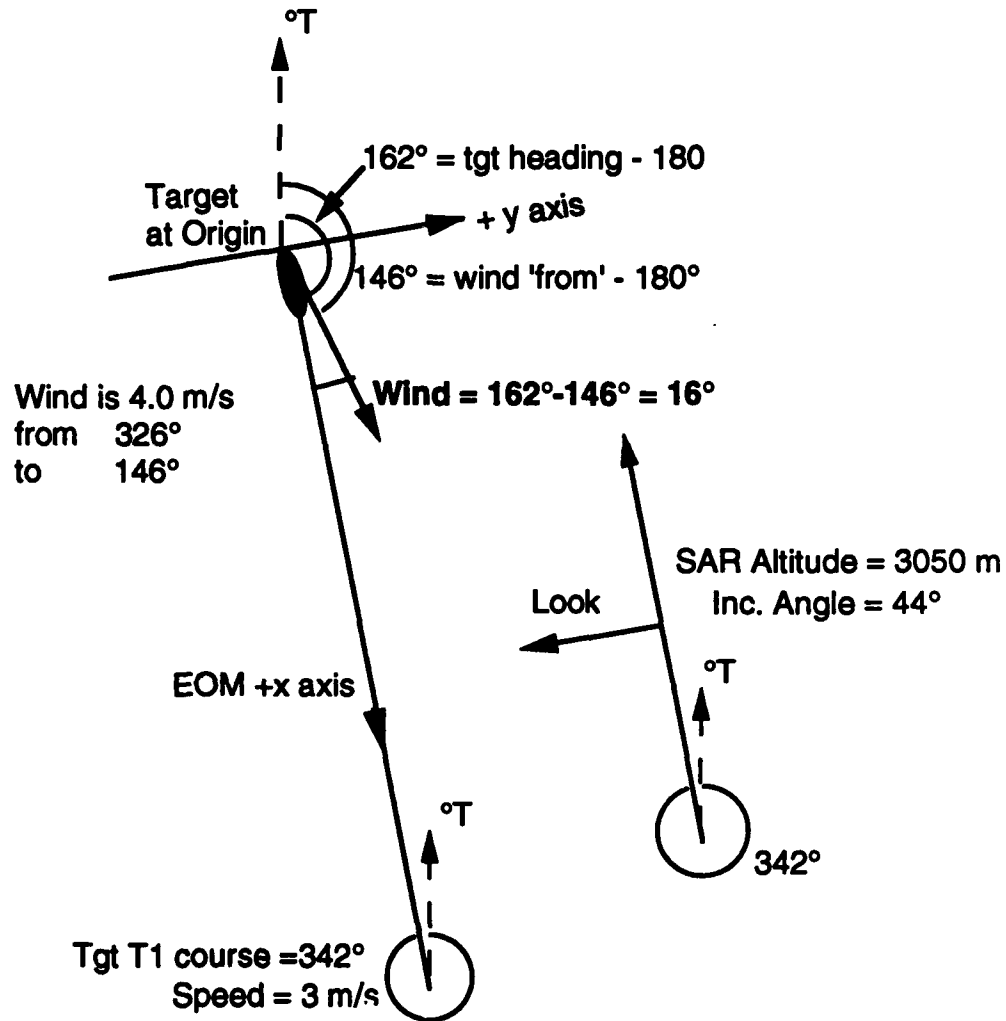
- Target at the origin
- Positive x-axis along wake
- Target travel in the -x direction

The EOM angles are defined as:

- $\text{ANGROT} = 270^\circ$ = angle of 'look' vector wrt x-axis (ccwise)
- $\text{WINDIR} = 232^\circ$ = angle of wind 'to' vector wrt x-axis (ccwise)

Figure B-2. EOM Geometry for 109-5

EOM Geometry for 115-3



The EOM X-axis is defined by:

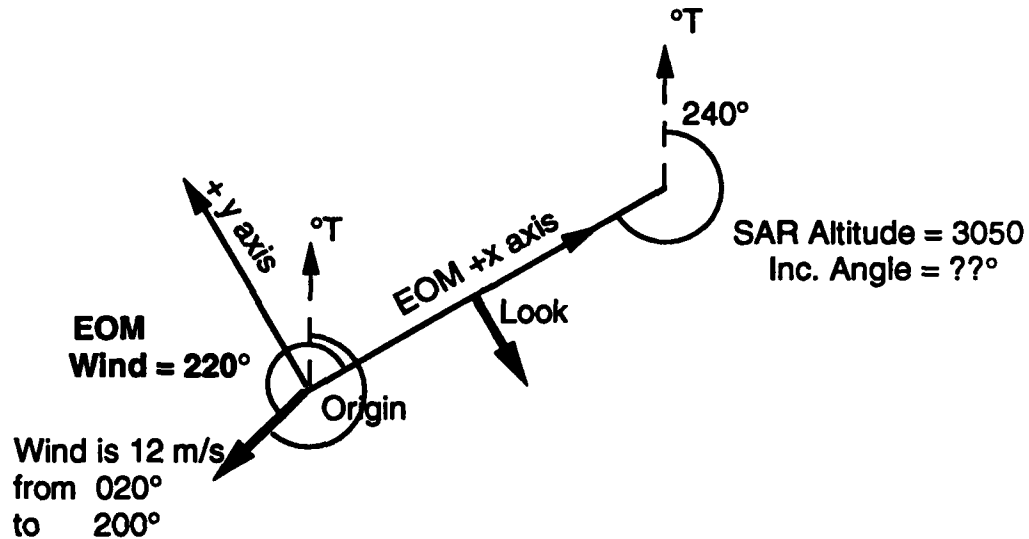
- Target at the origin
- Positive x-axis along wake
- Target travel in the -x direction

The EOM angles are defined as:

- $\text{ANGROT} = 270^\circ$ = angle of 'look' vector wrt x-axis (ccwise)
- $\text{WINDIR} = 16^\circ$ = angle of wind 'to' vector wrt x-axis (ccwise)

Figure B-3. EOM Geometry for 115-3

**EOM Geometry for 222-4
Non-standard case - no target
Use SAR track as x-axis**



The EOM X-axis is defined by:

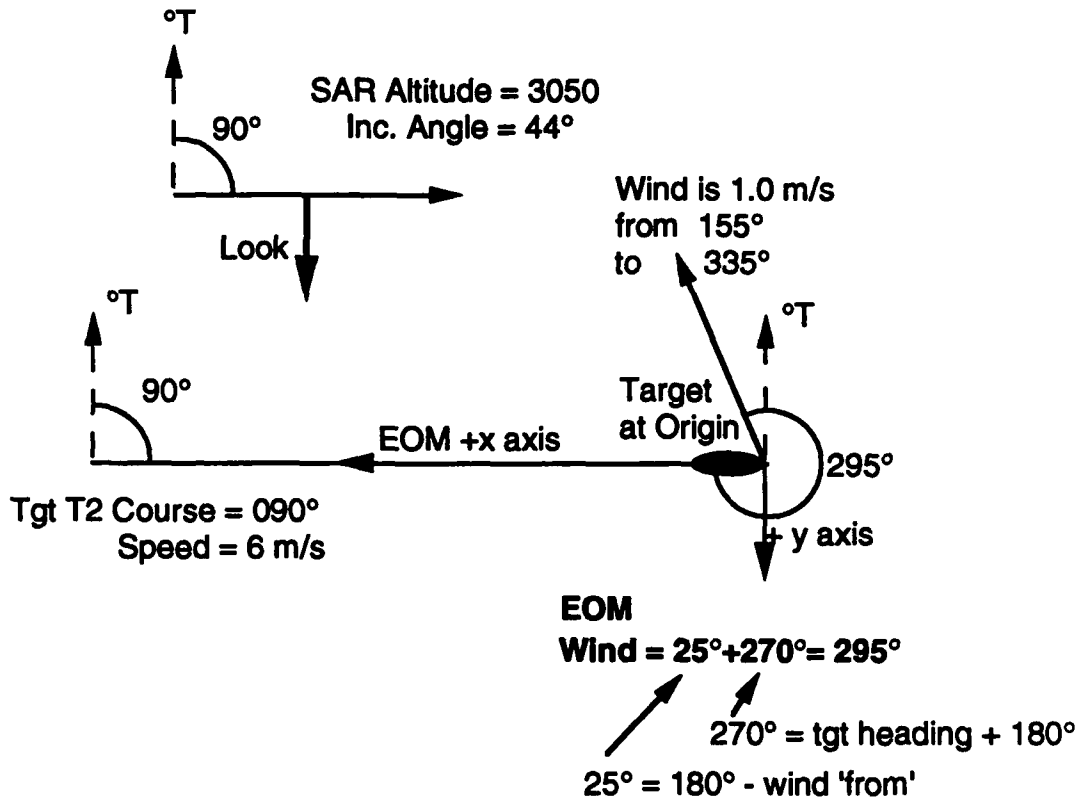
- SAR at the origin
- Positive x-axis along track
- SAR travel in the -x direction

The EOM angles are defined as:

- $ANGROT = 270^\circ$ = angle of 'look' vector wrt x-axis (ccwise)
- $WINDIR = 220^\circ$ = angle of wind 'to' vector wrt x-axis (ccwise)

Figure B-4. EOM Geometry for 222-4

EOM Geometry for 506-3



The EOM X-axis is defined by:

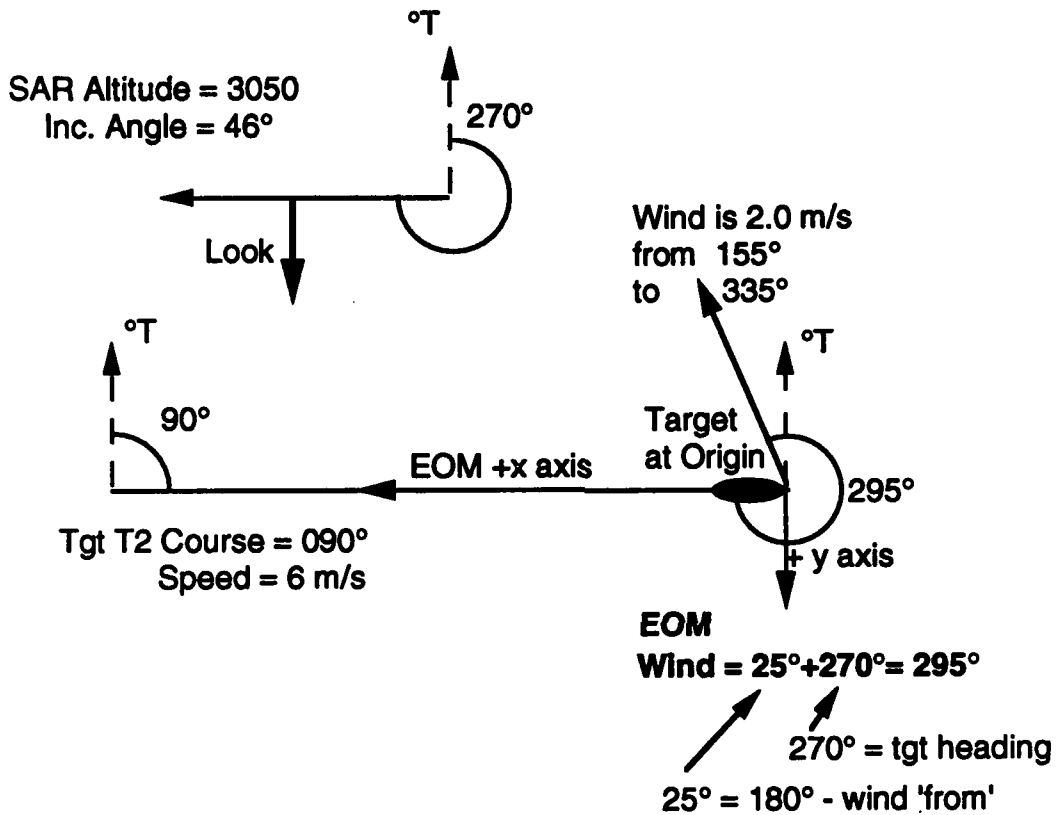
- Target at the origin
- Positive x-axis along track
- Target travel in the -x direction

The EOM angles are defined as:

- ANGROT = 90° = angle of 'look' vector wrt x-axis (ccwise)
- WINDIR = 295° = angle of wind 'to' vector wrt x-axis (ccwise)

Figure B-5. EOM Geometry for 506-3

EOM Geometry for 506-4



The EOM X-axis is defined by:

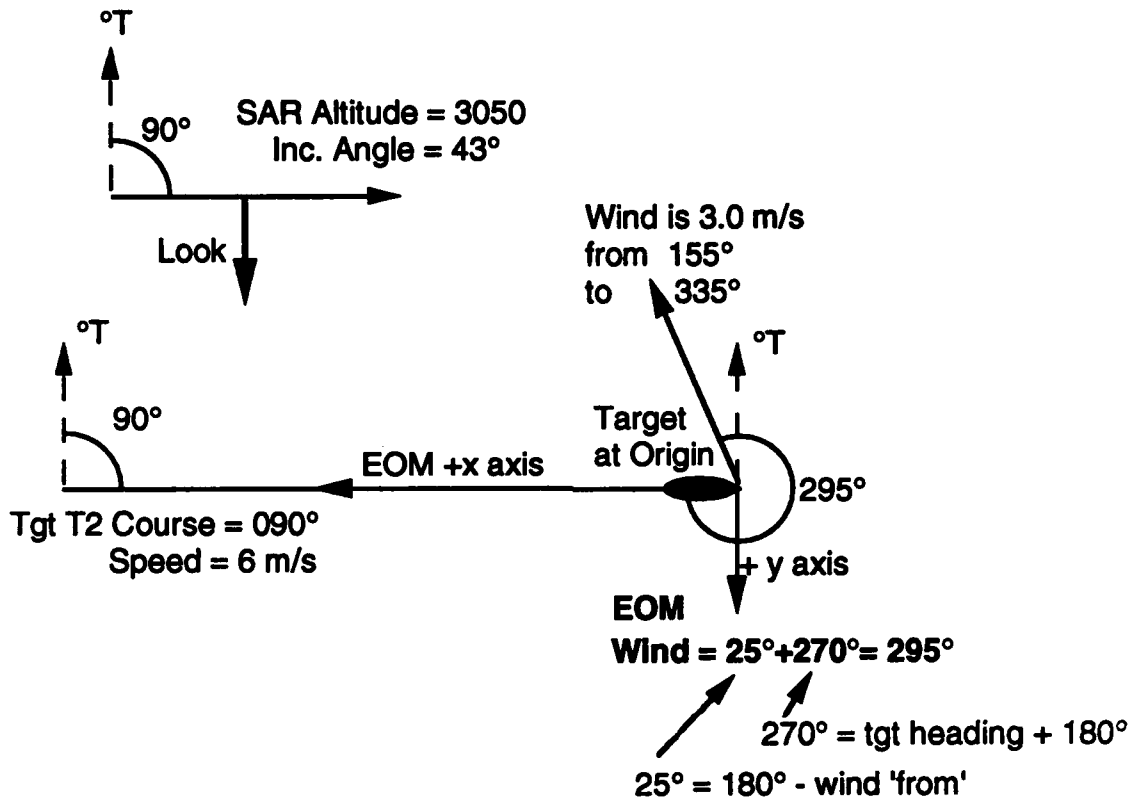
- Target at the origin
- Positive x-axis along wake
- Target travel in the -x direction

The EOM angles are defined as:

- ANGROT = 90° = angle of 'look' vector wrt x-axis (ccwise)
- WINDIR = 295° = angle of wind 'to' vector wrt x-axis (ccwise)

Figure B-6. EOM Geometry for 506-4

EOM Geometry for 506-5



The EOM X-axis is defined by:

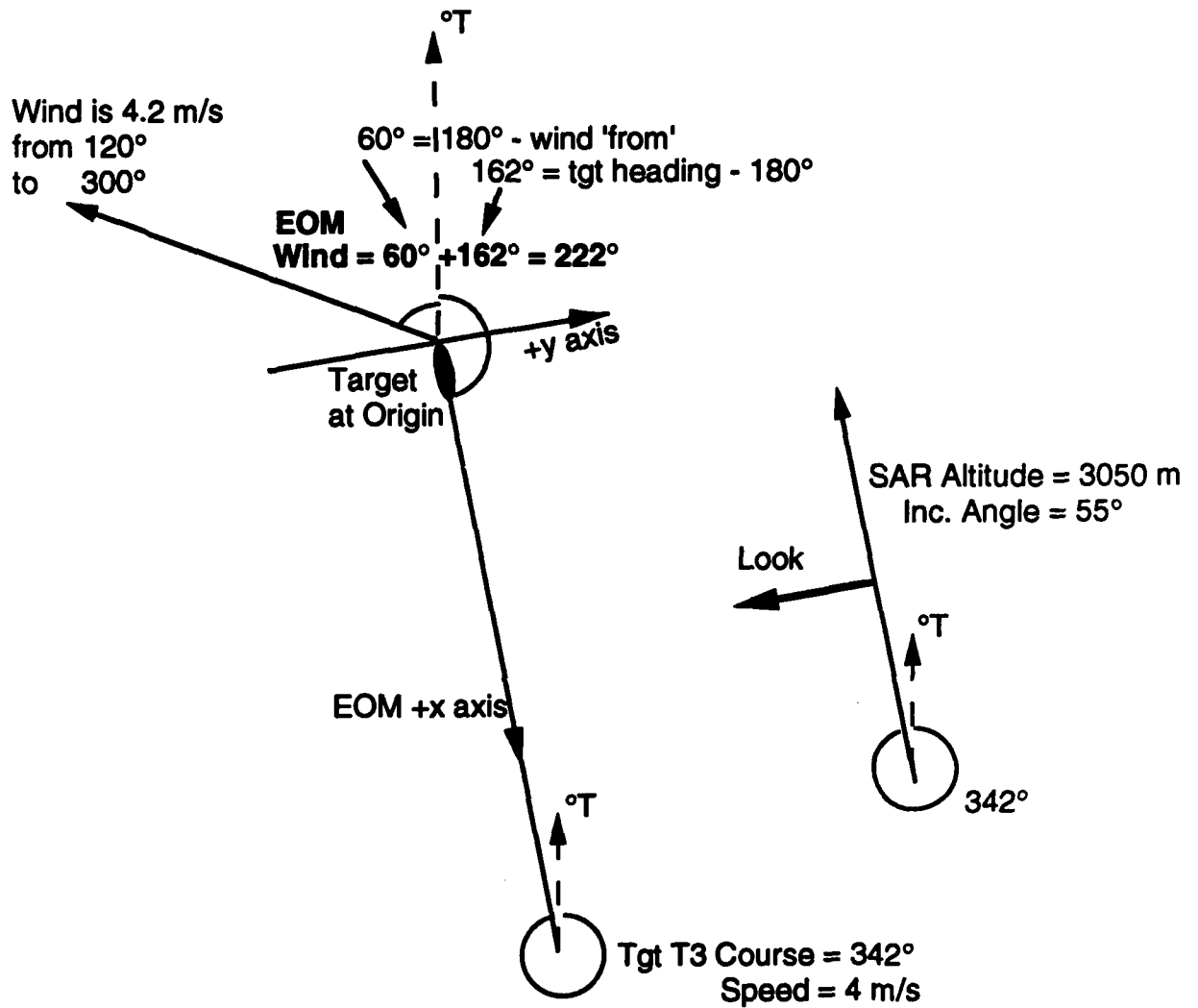
- Target at the origin
- Positive x-axis along wake
- Target travel in the -x direction

The EOM angles are defined as:

- ANGROT = 90° = angle of 'look' vector wrt x-axis (ccwise)
- WINDIR = 295° = angle of wind 'to' vector wrt x-axis (ccwise)

Figure B-7. EOM Geometry for 506-5

EOM Geometry for 914-4



The EOM X-axis is defined by:

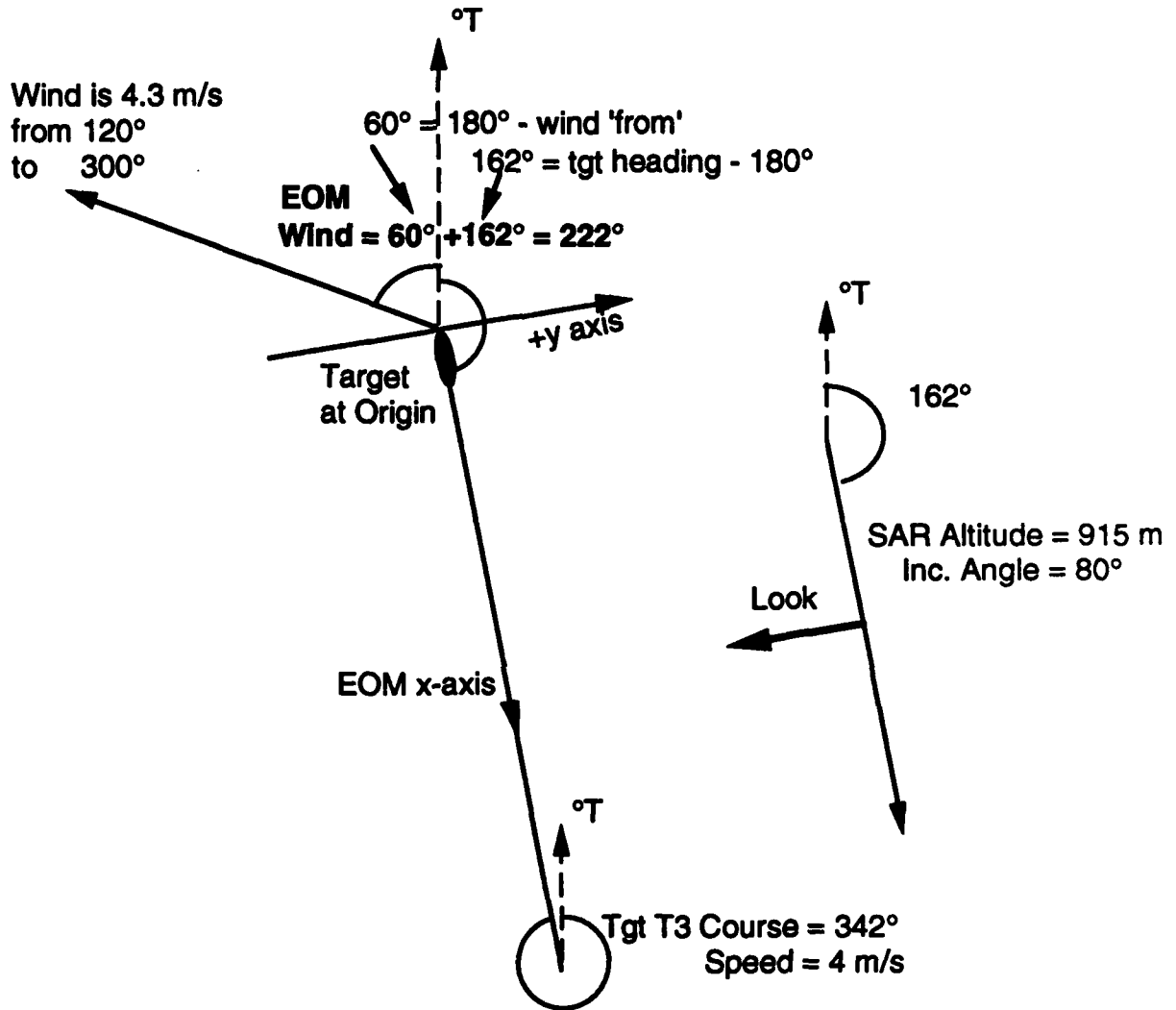
- Target at the origin
- Positive x-axis along track
- Target travel in the -x direction

The EOM angles are defined as:

- ANGROT = 270° = angle of 'look' vector wrt x-axis (ccwise)
- WINDIR = 222° = angle of wind 'to' vector wrt x-axis (ccwise)

Figure B-8. EOM Geometry for 914-4

EOM Geometry for 914-5



The EOM X-axis is defined by:

- Target at the origin
- Positive x-axis along track
- Target travel in the -x direction

The EOM angles are defined as:

- ANGROT = 270° = angle of 'look' vector wrt x-axis (ccwise)
- WINDIR = 222° = angle of wind 'to' vector wrt x-axis (ccwise)

Figure B-9. EOM Geometry for 914-5